Synoptic climatology of hybrid cyclones in the Australian region

J. F. Quinting[a, b*], J. L. Catto[a, c] and M. J. Reeder[a, d]

[a]*School of Earth, Atmosphere and Environment, Monash University, Clayton, Victoria, Australia*

[b]*Institute of Meteorology and Climate Research (IMK-TRO), Karlsruhe Institute of Technology (KIT), Karlsruhe, Germany*

[c]*College of Engineering, Mathematics and Physical Sciences, University of Exeter, Exeter, United Kingdom*

[d]*ARC Centre of Excellence for Climate Extremes, Monash University, Clayton, Victoria, Australia*

[*]Correspondence to: Institute of Meteorology and Climate Research (IMK-TRO), Karlsruhe Institute of Technology (KIT), POB 3640, 76021 Karlsruhe, Germany; Email: julian.quinting@kit.edu

In May and September 2016, two intense hybrid cyclones (HCs) developed over the Great Australian Bight damaging infrastructure and causing a state-wide power outage in South Australia. These two cyclones motivate the compilation of the first synoptic climatology of HCs in the Australian region, including an analysis of their importance for wind and precipitation extremes, and a composite view of the large-scale flow in which they develop. HCs are identified in ERA-Interim data from 1979 to 2010 using an objective feature tracking method and a cyclone phase space diagnostic. HCs exhibit a pronounced seasonal cycle with most of them occurring from May to September. During these months, HCs are most frequent over the Tasman Sea and the Great Australian Bight where they account for 50% of all cyclones. A common characteristic of all HCs is that the strongest precipitation, which is locally extreme in 91% of all HCs, falls in the warm-sector and along a bent-back warm front on the poleward side of the cyclones. Moreover, the area affected by extreme precipitation and the maximum precipitation in HCs are no different from non-hybrid cyclones (NHCs). In contrast, the area affected by extreme wind gusts is significantly larger in HCs than for NHCs. In both HCs and NHCs the strongest near-surface wind gusts typically occur in the cold air mass in the wake of the cyclones, especially in those over the Great Australian Bight. The upper-tropospheric structure of HCs is characterised by an elongated cyclonic potential vorticity anomaly embedded between two ridges that eventually cuts off. In contrast, NHCs are characterised by a zonal flow upstream and upper-tropospheric cyclonic wave breaking.

Key Words: Hybrid cyclone; subtropical cyclone; warm-seclusion cyclone; cyclone phase space

This article has been accepted for publication and undergone full peer review but has not been through the copyediting, typesetting, pagination and proofreading process, which may lead to differences between this version and the Version of Record. Please cite this article as doi: 10.1002/qj.3431

1. Introduction

In May and September 2016, two extratropical cyclones (ECs) developed explosively over the Great Australian Bight. The May cyclone affected the Eyre Peninsula and the Adelaide region with storm-force winds and a damaging storm surge along the coast (Bureau of Meteorology 2016a). The strong winds and the record high sea levels caused coastal erosion and damaged power lines, buildings and other infrastructure. The September cyclone and its associated cold front affected nearly the same region with destructive winds, intense rainfall and an outbreak of severe thunderstorms including hail and at least seven tornadoes (Bureau of Meteorology 2016b). The winds severely damaged the South Australian power network resulting in a state-wide power outage (Bureau of Meteorology 2016b; Lucas 2017). According to the Bureau of Meteorology, the cyclone produced the lowest sea level pressure recorded at a weather station in South Australia at a standard observation time (972.7 hPa at Neptune Island). Both cyclones were characterised by an upper-tropospheric cold core and a shallow lower-tropospheric warm core, and are thus defined as hybrid cyclones (HCs). They provide the motivation for the present study, which is to document the climatological structure and evolution of HCs in the Australian region.

Extratropical cyclones are usually asymmetric and derive their energy from baroclinic energy conversion. Although ECs are typically characterised by an upper-level cold core, they may develop either a lower-tropospheric warm core or a lower-tropospheric cold core. ECs exhibiting a lower- and upper-troposperic cold core are referred to as non-hybrid cyclones (NHCs) in this study. The fraction of ECs exhibiting a lower-tropospheric warm core varies regionally but may be significant (Čampa and Wernli 2012). For the northwestern hemisphere, Hart (2003) estimated that 10–15% of ECs develop both an upper-tropospheric cold core and a lower-tropospheric warm-core during their lifecycle. These cyclones are referred to as HCs. The most prominent example of midlatitudes HCs are warm-seclusion cyclones which constitute the mature stage of the Shapiro and Keyser (1990) lifecycle paradigm. Further examples of HCs are extratropical transitioning TCs (e.g., Jones *et al.* 2003; Evans *et al.* 2017), tropical transitioning disturbances originating from the midlatitudes (e.g., Davis and Bosart 2004; McTaggart-Cowan *et al.* 2013), and subtropical cyclones (e.g., Simpson 1952; Evans and Guishard 2009). Since the present study mainly considers subtropical cyclones and warm-seclusion cyclones, we briefly recapitulate their main characteristics in the following.

In their influential book chapter, Shapiro and Keyser (1990) integrated the results of observational and numerical studies into a new conceptual model for the life cycle of marine extratropical frontal cyclones. In their model, cyclogenesis begins along a continuous and broad low-level baroclinic zone, with fronts developing as the cyclone intensifies. In contrast to the Norwegian cyclone model (Bjerknes and Solberg 1922), where the cold front merges with the warm front to form an occluded front, the cold front moves perpendicular to the warm front forming a frontal T-bone. As the cyclone approaches its mature phase, the temperature gradient related to the warm front is advected cyclonically around the cyclone centre (e.g., Takayabu 1986; Neiman and Shapiro 1993; Schultz *et al.* 1998), forming a bent-back warm front. This bent-back warm front wraps around the cyclone centre, enclosing a pocket of relatively warm air that is encircled by cold polar air. Shapiro and Keyser (1990) referred to this pocket of warm air which forms a lower-tropospheric warm core at the mature stage of the cyclone as a warm seclusion. Since then, the dynamics of these cyclones have been investigated in idealised models (e.g., Snyder *et al.* 1991; Hines and Mechoso 1993; Reed *et al.* 1994; Schultz *et al.* 1998) and in observations (e.g., Neiman and Shapiro 1993; Grønås 1995).

Subtropical cyclones form over many ocean basins, including the subtropical Pacific (e.g., Simpson 1952; Otkin and Martin 2004), the Atlantic (e.g., Guishard *et al.* 2009; Evans and Braun 2012), and the Tasman Sea (e.g., Holland *et al.* 1987; Garde *et al.* 2010; Browning and Goodwin 2013; Cavicchia *et al.* 2018). On the large-scale, subtropical cyclogenesis is typically preceded by a meridionally-elongated stratospheric intrusion of cyclonic potential vorticity (PV), often referred to as a PV streamer (e.g., Caruso and Businger 2006; Moore *et al.* 2008; Garde *et al.* 2010). This streamer eventually becomes detached from the stratospheric cyclonic PV reservoir, resulting in a cut-off which forces ascent in a weakly stable large-scale environment. The deep vertical ascent in a region of weak static stability is associated with convection

that generates lower-tropospheric PV through latent heating and hence contributes to the subtropical cyclogenesis (e.g., Caruso and Businger 2006). Vigorous ascent typically occurs on the poleward and eastern side of these cyclones in a baroclinic environment (e.g., Simpson 1952; Davis and Bosart 2004; Hulme and Martin 2009; Cordeira and Bosart 2011; Bentley and Metz 2016; Cavicchia *et al.* 2018) which bears similarities with bent-back warm fronts characteristic of the Shapiro and Keyser (1990) cyclone model. In the present study, no distinction is made between subtropical cyclones and warm-seclusion cyclones. Henceforth, the term HC encompasses both cyclone types.

The most prominent and widely studied cyclones in the Australian region are known as East Coast Lows, which form in a maritime environment in the vicinity of the east coast of Australia (e.g., Holland *et al.* 1987; Speer *et al.* 2009). These cyclones, particularly those that are most intense, possess structures characteristic of HCs: East Coast Lows tend to be associated with pronounced upper-level cyclonic PV anomalies that extend into the subtropics and eventually cut-off from the main stratospheric PV reservoir (Mills *et al.* 2010; Garde *et al.* 2010; Dowdy *et al.* 2013; Cavicchia *et al.* 2018). The subtropical jet lies on the equatorward flank of these cyclonic anomalies and may be accompanied by a north-west cloud band (Downey *et al.* 1981) and a subtropical surface front. The cyclogenesis is well poleward of the subtropical front over a weaker second baroclinic zone in the southern part of the continent. In agreement with the Shapiro and Keyser (1990) cyclone model, a bent-back warm front on the poleward side of the low pressure systems is accompanied by convection which may cause heavy rain (Mills *et al.* 2010).

Although strong surface-winds and heavy precipitation in regions beyond the east coast of Australia have been linked to HCs (Mills and Wu 1995; Griffiths *et al.* 1998; Qi *et al.* 1999; Mills 2001; Qi *et al.* 2006; Garde *et al.* 2010), only a handful of studies have analysed their dynamics and a comprehensive synoptic-climatological investigation of this type of cyclone is missing. Motivated by the two HCs of 2016, the present study addresses the following questions

- What is the seasonal distribution of HCs in the Australian region?
- What fraction of cyclones in the region are HCs? And how does this fraction differ between the Great Australian Bight and the Tasman Sea?
- In terms of precipitation and near-surface winds, are HCs more extreme than NHCs?
- Do HCs develop in a particular large-scale flow configuration? And does this configuration differ from that in which other NHCs form?

The data and methods to compile the climatology are introduced in Section 2. The two HC developments in May and September 2016 are discussed in Section 3. The synoptic climatology of HCs in the Australian region in Section 4 includes an analysis of the precipitation and near-surface wind extremes, and the flow configuration in which HCs develop. A concluding discussion and outlook are presented in Section 5.

2. Data and methodology

All analyses in the present study are based on 6-hourly ERA-Interim reanalyses (Dee *et al.* 2011) regridded to a uniform 0.75° latitude–longitude grid. Following Catto and Pfahl (2013), six-hourly accumulated precipitation data are taken from the 0–6 h and 6–12 h ERA-Interim forecast fields that are initialised at 00 and 12 UTC. Information concerning wind gusts associated with the cyclones is also taken from ERA-Interim data. The wind gusts in ERA-Interim are based on the resolved 10-m wind speed and an empirical multiplier from the turbulence scheme that is designed to capture the effects of surface friction and stability (ECMWF 2007). The two case studies are augmented with infrared satellite imagery derived from the GridSat-B1 data (Knapp *et al.* 2011).

2.1. *Cyclone tracking*

The methods described in Hodges (1994, 1995, 1999) and Hoskins and Hodges (2002, 2005) are used here to identify and track the cyclones. In brief, the cyclone centres are defined as minima in the 850-hPa relative vorticity field (in the Southern Hemisphere) truncated to a T42 Gaussian grid. The tracks are constructed from the cyclone centres using a simple nearest neighbour approach, then by minimizing a cost function, the most likely tracks are produced. To ensure that the cyclones are mobile,

the tracks must last at least 2 days and be at least 1000 km long. The present study focuses on cyclones that were located at least once during their life cycle between 20–50°S and 100–180°E and reached a peak intensity of less than -6×10^{-5} s^{-1} (greater than 6 cyclonic vorticity units; CVU) at 850 hPa.

2.2. *Cyclone phase space*

HCs are identified using the cyclone phase space diagnostic of Hart (2003) and Evans and Hart (2003). Three parameters describing the general structure of cyclones define the phase space. The first parameter is the lower-tropospheric thermal asymmetry B, which is defined as the storm-motion-relative 900–600-hPa thickness asymmetry within 500 km of the cyclone centre. The storm motion is calculated as the difference between the current cyclone position and its position 6 hours before. B is approximately zero for highly symmetric cyclones such as TCs or occluded ECs, but large and positive for developing ECs. The remaining two parameters are the lower-tropospheric thermal wind $-V_T^L$, and the upper-tropospheric thermal wind $-V_T^U$. These parameters distinguish cold-core from warm-core structures. $-V_T^L$ is defined as the vertical derivative of the cyclone height perturbation $\Delta Z = Z_{max} - Z_{min}$ between 900 and 600 hPa within a 500-km radius of the centre. Likewise, $-V_T^U$ is defined as the vertical derivative of the cyclone height perturbation between 600 and 300 hPa. A linear regression fit to the vertical profile in ΔZ at increments of 50 hPa ensures a unique magnitude and sign for $-V_T^L$ and $-V_T^U$ even in non-linear vertical profiles of the cyclone height perturbation (Hart 2003). Negative values of $-V_T^L$ ($-V_T^U$) indicate a low-level (upper-level) cold-core, whereas positive values indicate a low-level (upper-level) warm-core. Cold-core ECs are characterised by negative $-V_T^L$ and $-V_T^U$, though warm-core TCs exhibit positive $-V_T^L$ and $-V_T^U$. By definition, HCs have positive values of $-V_T^L$, implying a larger perturbation at 900 hPa than at 600 hPa, a positive thermal wind, and stronger near-surface wind. $-V_T^U$ is generally negative in HCs, with only the most intense cyclones (those with minimum central pressures below 940 hPa) having slightly positive $-V_T^U$ values (Hart 2003). With these considerations in mind, HCs are defined here as cyclones for which $B < 10$, $-V_T^L > 0$ and $-V_T^U < 0$ at their time of peak intensity. Choosing $B < 10$ instead of $B = 0$ accounts for the effects of cyclone tracking uncertainties, small-scale storm asymmetries and data analysis uncertainties which can lead to slightly positive/negative values of B even in mature TCs (Hart 2003). The requirements $-V_T^L > 0$ and $-V_T^U < 0$ follow the definition of subtropical cyclones in Guishard *et al.* (2009) and are in the range of previous studies on HCs (e.g., Evans and Braun 2012; Yanase *et al.* 2014; González-Alemán *et al.* 2015).

3. Two illustrative hybrid cyclones

The explosive development of the cyclones in May and September 2016, and their effect on the weather in South Australia provide the motivation for the present study. In the following, the development of the two cyclones is described.

3.1. *Cyclone phase space for the two hybrid cyclones*

The cyclone phase space trajectories for the May and September 2016 cyclones are shown in Fig. 1. As is typical of developing cyclones, the two cyclones possess an asymmetric deep cold-core (upper left quadrant in Fig. 1a, lower left quadrant in Fig. 1b) during the early stages of their life cycle. At the time of their lowest mean sea level pressures on 8 May and 28 September, the cyclones have symmetric shallow warm-cores (lower right quadrants in Figs. 1a, b), and consequently both cyclones are HCs. After reaching peak intensity, the May cyclone develops an asymmetric deep cold core lasting until 1200 UTC 9 May, whereas the September cyclone develops a symmetric deep cold core lasting until the end of its life cycle.

3.2. *The May 2016 cyclone*

Two days before the explosive cyclogenesis over the Great Australian Bight on 7 and 8 May, the midlatitude flow is characterised by an upper-level ridge over the eastern South Indian Ocean and a broad trough south of Australia (not shown). At 0600 UTC 7 May an upper-tropospheric PV streamer extends equatorward to western Australia (blue contours in Fig. 2a), which is presumably a response to the strong equatorward flow on the eastern flank of the upstream ridge. At the same time, a broad region of low sea level pressure (red contours in Fig. 2d) marks a shallow cyclone ahead of this streamer in the equatorward

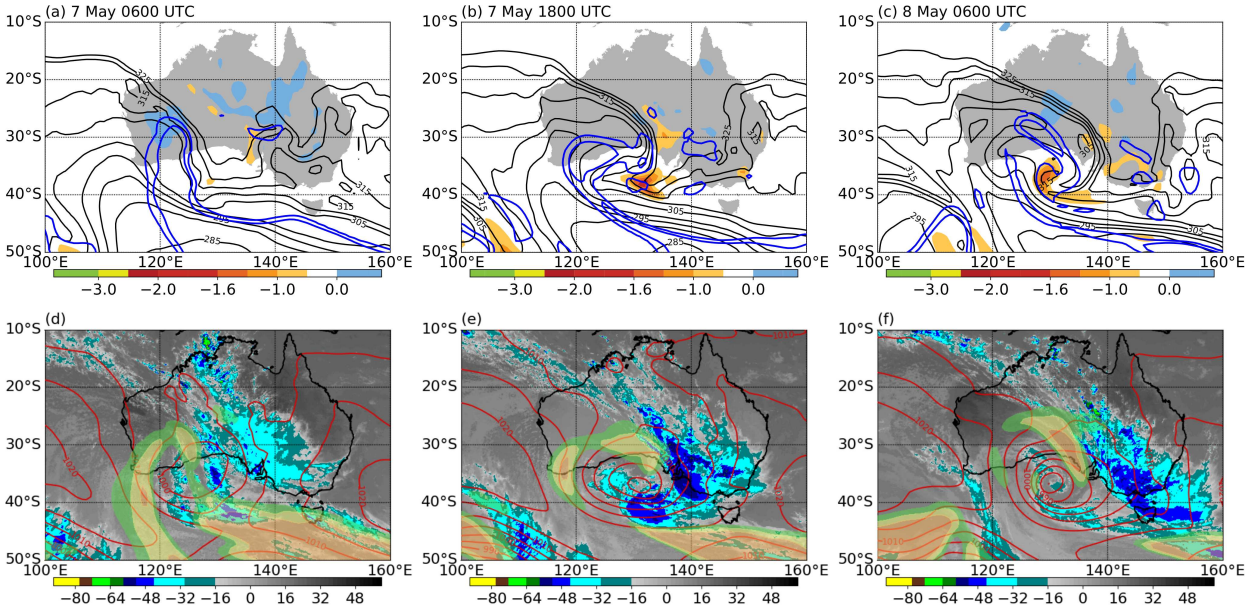

Figure 2. Development of the May cyclone between 0600 UTC 7 May and 0600 UTC 8 May. (a, b, c) 315-K PV (blue contours at −1, −2 PVU), 950–750-hPa mean PV (shading in PVU), and 950–750-hPa mean equivalent potential temperature (black contours in K). (d, e, f) brightness temperature of the false-colour infrared satellite imagery (°C; shading) derived from the GridSat-B1 data set, 315-K wind speed (semi-transparent shading at $30, 35, 40\,\mathrm{m\,s^{-1}}$), and sea level pressure (red contours in hPa).

entrance region of the midlatitude jet (semi-transparent shading in Fig. 2d). The low pressure system is associated with two frontal zones in the lower troposphere. A pronounced gradient in equivalent potential temperature (black contours in Fig. 2a) marks the cold frontal zone that extends from the low pressure area northwestward over subtropical Australia. The second frontal zone, as marked by the equivalent potential temperature gradient, extends eastward across the Great Australian Bight. Thus, the two frontal zones delineate a warm-sector over central and eastern Australia (shading in Fig. 2d). In this warm-sector, the satellite imagery reveals a cloud band extending from north to southeast Australia. Generally, the synoptic setup is very similar to that of a HC development described in Griffiths *et al.* (1998).

The low-pressure system deepens to a central minimum pressure of less than 990 hPa by 1800 UTC 7 May (Fig. 2e). This intensification is accompanied by the development of high-level clouds as indicated by low brightness temperatures (Fig. 2e) and the formation of low-level cyclonic PV anomalies at the southern tip of the warm sector (shading in Fig. 2b). The development of high-level clouds characterises the period of explosive cyclogenesis that continues until 0600 UTC 8 May. According to the Bureau of Meteorology's manual analyses*, the mean sea level pressure falls from 997 hPa at 0600 UTC 7 May to 978 hPa at 0600 UTC 8 May. At a latitude of about 36°S, this deepening rate corresponds to more than one Bergeron†, and consequently fulfils the "bomb" criterion for explosive development (Sanders and Gyakum 1980).

This explosive development, which bears many similarities with the Shapiro–Keyser cyclone model (Shapiro and Keyser 1990), is also depicted in the mean sea level pressure field of the reanalysis data. The central pressure falls to 980 hPa at 0600 UTC 8 May (Fig. 2f). As is characteristic for a Shapiro–Keyser cyclone, the movement of the cold front over the Australian continent is nearly perpendicular to the warm frontal zone over the Great Australian Bight, forming a frontal T-bone structure with a bent-back warm front extending westward of the cyclone centre and a frontal fracture close to the cyclone centre (Figs. 2b, c). In association with the rapid intensification, the low-level PV decreases to less than -1.5 PVU (Figs. 2b, c). The collocation of the cyclonic PV, tropospheric-deep ascent (not shown), and the high-level clouds suggests that latent heating contributes to the cyclone intensification.

In the mid- to upper-troposphere, the cyclone intensification is accompanied by a LC1-type wave breaking (Thorncroft *et al.* 1993) and a cyclonic wrap-up of the PV streamer (Figs. 2b, c). This wrap-up is reflected in the satellite image as a cloud-free

*The manual analyses are available online at http://www.bom.gov.au/australia/charts/archive/index.shtml

†1 Bergeron = 24 hPa (sin ϕ/sin 60) where ϕ is the latitude of the cyclone centre.

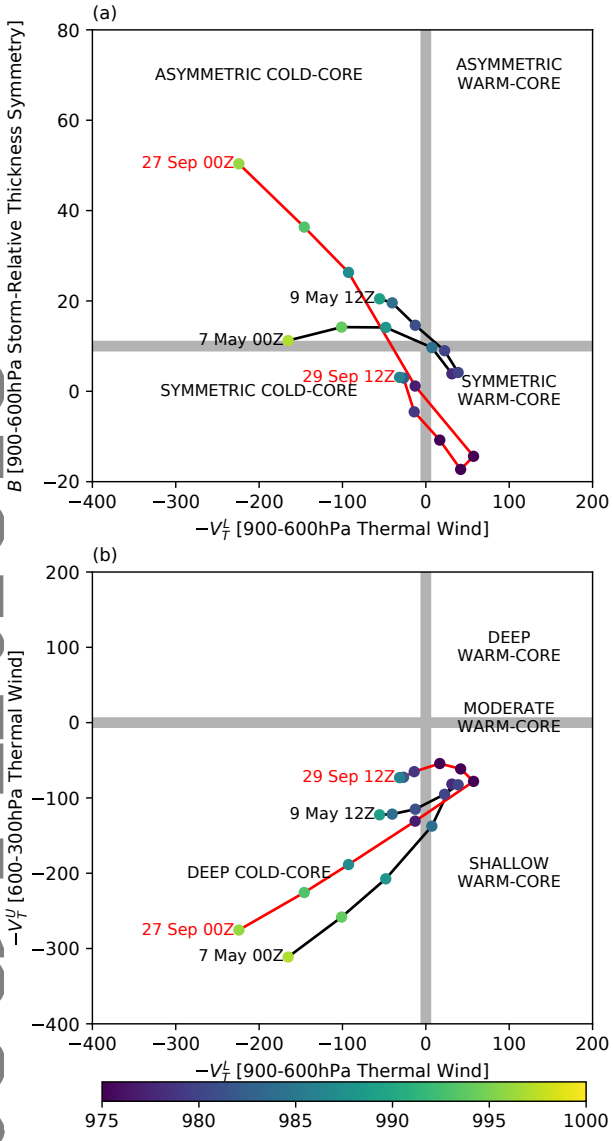

Figure 1. Cyclone phase space diagram for the May cyclone (black line) and the September cyclone (red line). Phase evolution: (a) $-V_T^L$ vs B and (b) $-V_T^L$ vs $-V_T^U$. A marker is placed every 6 h and the shading of each marker indicates the cyclone mean sea level pressure in hPa.

area that spirals toward the cyclone centre (Fig. 2f). At 0600 UTC 8 May, the leading edge of the PV streamer is collocated with the low-level cyclonic PV along the warm front. Thus, the two cyclonic PV anomalies form a vertically stacked and troposphere-spanning PV-tower which is characteristic of the mature stage of cyclone development (e.g., Rossa *et al.* 2000; Wang and Rogers 2001; Čampa and Wernli 2012).

Characteristic of the Shapiro–Keyser cyclone model, a pool of relatively warm air in the cyclone centre is the warm-seclusion (Fig. 2c). In the satellite image, the cyclone centre is detached from the northwest cloud band and it has a symmetric structure with a cloud-free area reaching the cyclone centre. Consistent with the Shapiro–Keyser cyclone model the cyclone deepening terminates shortly after the development of the warm-seclusion at 0600 UTC 8 May.

3.3. *The September 2016 cyclone*

The large-scale synoptic pattern prior to the cyclone development in September 2016 is similar to that in May 2016. The flow at 315 K is characterised by an upper-level ridge over the eastern South Indian Ocean and a trough to the south of western Australia (Fig. 3a). Ahead of the axis of this trough and on the poleward side of the upper-level jet, a secondary low starts to develop at 0600 UTC 27 September as indicated by a local mean sea level pressure minimum of less than 1000 hPa at 120°E and 36°S (Fig. 3d). To the south and west of the pressure minimum, low brightness temperatures indicate high-level clouds (Fig. 3d) related to ascent in a region of a low-level baroclinic zone (Fig. 3a). The proximity of this cloud-feature to open cellular convection in the cold air and its location on the poleward side of the upper-level jet indicates an instant-occlusion type cyclogenesis (e.g., Zillman and Price 1972; Browning and Hill 1985; Evans *et al.* 1994), very similar to the cyclone investigated in Griffiths *et al.* (1998).

Still located ahead of the axis of the upper-level trough at 315 K, the low pressure system deepens to less than 985 hPa at 1800 UTC 27 September (Figs. 3b, e). The period of intensification is accompanied by an expansion of the high-level clouds mostly to the south of the low pressure system. As for the May cyclone, the area of high-level clouds is collocated with a warm frontal zone as shown by the lower tropospheric gradient in equivalent potential temperature. On the triple point between the warm and the cold front, a negative low-level PV anomaly of less than –1 PVU develops.

The intensification continues until 0600 UTC 28 September. According to the Bureau of Meteorology's manual analysis, the mean sea level pressure reaches 973 hPa. The mean sea level pressure falls within 24 h from 1000 to 973 hPa, exceeding 1 Bergeron. As for the May cyclone, the low pressure system strongly resembles a Shapiro–Keyser cyclone. At this time a bent-back warm front extends from west of the cyclone to its southeast (Fig. 3c), which is collocated with an elongated negative PV anomaly that is strongest in the cyclone centre. A pronounced cold front, extending from the cyclone to northwestern Australia,

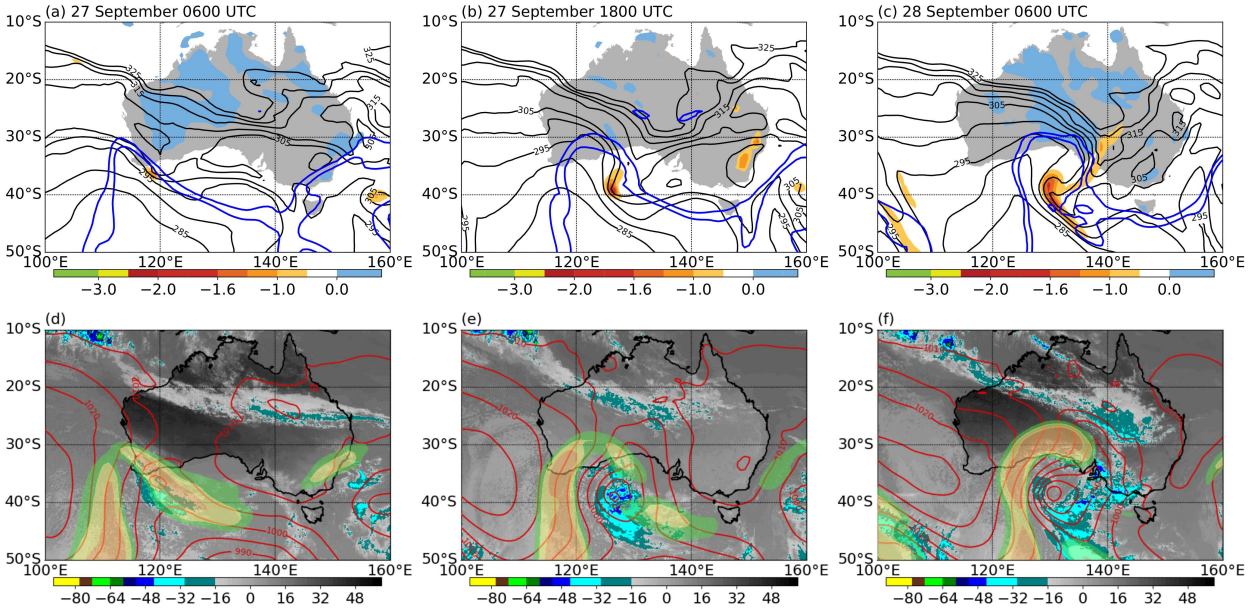

Figure 3. As Fig. 2, but for September cyclone between 0600 UTC 27 September and 0600 UTC 28 September . (d, e, f) Semi-transparent shading of the 315-K wind speed at 40, 45, 50 m s^{-1}.

moves perpendicular to the bent-back warm front. Relatively low brightness temperatures in the infrared satellite image over South Australia indicate deep convection along the cold front (Fig. 3f), coinciding with thunderstorms, hail and tornadoes at around this time (Bureau of Meteorology 2016b), which led to the state-wide power outage in South Australia.

4. Synoptic climatology

4.1. Climatological distribution

From 1979 to 2010, 1014 HCs reaching a peak intensity of at least 6 CVU at 850 hPa were identified between 20 to 50°S and 100 to 180°E. Although HCs occur all year round, their frequency exhibits a pronounced seasonal cycle (black bars in Fig. 4a). About two HCs per month occur from November to April. The number of HCs peaks in Southern Hemisphere winter with up to four cyclones per month in July. The frequency of NHCs exhibits a seasonal cycle too (grey bars in Fig. 4a). However, it is much less pronounced so that the fraction of HCs relative to NHCs is larger during winter than during summer. This is particularly noticeable for the Tasman Sea (see white lines in Fig. 4b for definition of the Tasman Sea and Great Australian Bight). In all seasons except for winter, NHCs are more frequent in the Tasman Sea than HCs (cf. hatched blue bars and filled blue bars in Fig. 4a). In Southern Hemisphere winter, however, HCs amount to roughly 50% of all ECs in the domain considered. During July, they occur even twice as frequent than NHCs. Likewise, HCs over the Great Australian Bight occur as frequently as NHCs in June and July (cf. filled red bars and hatched red bars in Fig. 4a).

Table 1. Number of HCs and NHCs reaching their peak intensity during MJJAS in the region 20 to 50°S and 100 to 180°E and for three different regions.

	total	Great Australian Bight	Tasman Sea	East Coast Low region
HCs	573	41	141	61
NHCs	2248	46	151	51

Given that HCs occur most frequently during May to September and that the two case studies occurred during these months, the remaining analyses in this paper focus on HCs identified during extended winter May to September (MJJAS). In total, 573 HCs were identified in the region 20 to 50°S and 100 to 180°E during MJJAS (Table 1). With 2248 NHCs during the same period, every fifth cyclone occurring in this region is a HC. However, the fraction of HCs compared to NHCs varies substantially depending on the region of interest. In the region of the climatologically highest cyclone frequency (black contours in Fig. 4b) between 100 to 120°E and 40 to 50°S, the number of HCs is comparatively low (shading in Fig. 4b). HCs occur most frequently over the Tasman Sea and the Great Australian Bight with locally more than two cyclones per month during MJJAS (Fig. 4b). At the time of peak intensity, 41 (141) HCs were located over the Great Australian Bight (Tasman Sea) from 1979 to 2010.

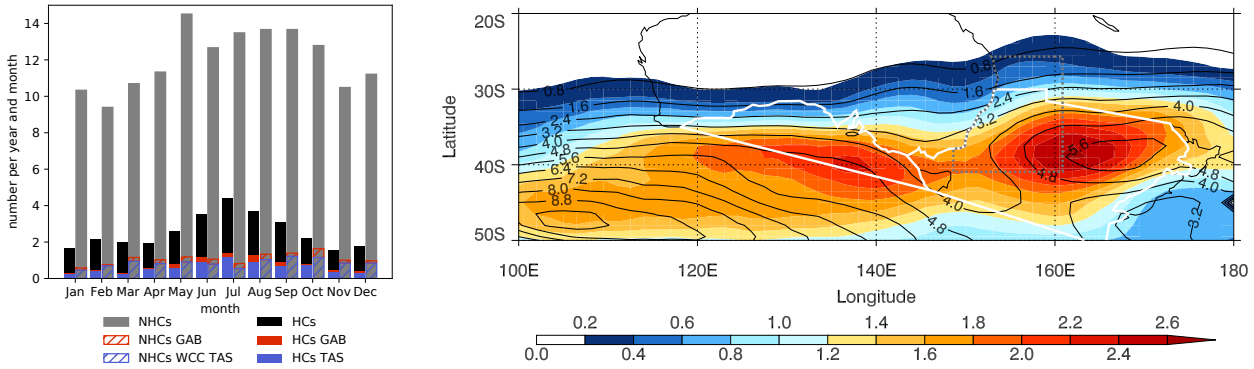

Figure 4. (a) Monthly distribution of HCs (black bars) and NHCs (grey bars) per year and month at their time of peak intensity. Blue and red bars denote the seasonal distribution of cyclones over the Tasman Sea (TAS) and Great Australian Bight (GAB), respectively. (b) Number of HC tracks (shading) and number of all cyclone tracks, i.e., HCs and NHCs (black contours), per month and 5° spherical cap for MJJAS. The white lines denote the Great Australian Bight and the Tasman Sea, respectively. The dashed grey line marks the East Coast Low region.

During the same period, 46 (151) NHCs occurred over these two ocean basins. Thus, almost every second cyclone in these two sub-regions is a HC.

Of special interest in Australia, is the East Coast Low (ECL) region since cyclones developing in this area can cause major damage to the coast line of eastern Australia. The ECL region is bounded by the Australian coast line, 161°E, 24°S, and 41°S (see Pepler *et al.* (2017b) for details). During MJJAS 1979–2010, 61 HCs and 51 NHCs reached their peak intensity in this region. Thus, more than half of all cyclones reaching their peak intensity in the ECL region are HCs. That a large fraction of HCs develop in this region, raises the question as to how many ECLs are also HCs. Taking the ERA-Interim based objective data set of Pepler *et al.* (2017b), the cyclone phase space diagnostic is applied to all ECLs. The main finding is that 46% of all ECLs during MJJAS fulfil the HC criteria defined in Section 2.2 at least once during their lifecycle.

4.2. Precipitation and wind extremes

Although storm-force winds and heavy rain have been linked to HCs in the Australian region in several case studies (e.g., Griffiths *et al.* 1998; Mills 2001; Qi *et al.* 2006; Mills *et al.* 2010), a general picture of how HCs are linked to precipitation and wind extremes is missing. Where the most extreme precipitation and wind gusts occur relative to the cyclone centre at peak intensity is also unknown. To study the link between HCs and these extremes and to compare them against NHCs, we first compute at each grid point the 99th percentile of the 6-hourly accumulated precipitation and 10-m wind gusts for each month in the period 1979–2010. Values exceeding the 99th percentile at each grid point are defined as extreme. By first masking the area around each cyclone we can attribute the extremes to a specific cyclone. Following Pfahl and Wernli (2012), the mask is defined as the area enclosed by the outermost closed mean sea level pressure contour that contains the cyclone centre. Since the analysis is performed at the time of peak intensity, all cyclones have a closed pressure contour. The major advantage of such a definition is that no a priori assumptions about the cyclone radius are made. Starting from the cyclone centre, the closed contours are identified at intervals of 0.5 hPa up to a maximum length of 7500 km. Grid points of extreme precipitation or wind that lie within the cyclone mask are attributed to the cyclone. Performing the same analysis 12 hours prior to the time of peak intensity does not affect the main conclusions (not shown).

According to a Mann-Whitney-U test, the distributions of the 6-hourly maximum precipitation attributable to all HCs and all NHCs (Fig. 5a) do not differ significantly. The interquartile range of the maximum 6-hourly precipitation related to HCs and NHCs extends from 9–19 mm and from 5–15 mm, respectively. The extreme precipitation values for cyclones over the Tasman Sea is notably different from those over the Great Australian Bight. The average maximum 6-hourly precipitation exceeds 20 mm and the 99th percentile reaches 70 mm for HCs over the Tasman Sea. The range of maximum 6-hourly precipitation for cyclones over the Great Australian Bight is significantly lower. On average, the maximum 6-hourly precipitation is about 15 mm and the 99th percentile reaches 25 mm. Both cyclones in May and September 2016 exceeded this 99th percentile (red and black star in Fig. 5a). Although the 6-hourly precipitation maxima are significantly

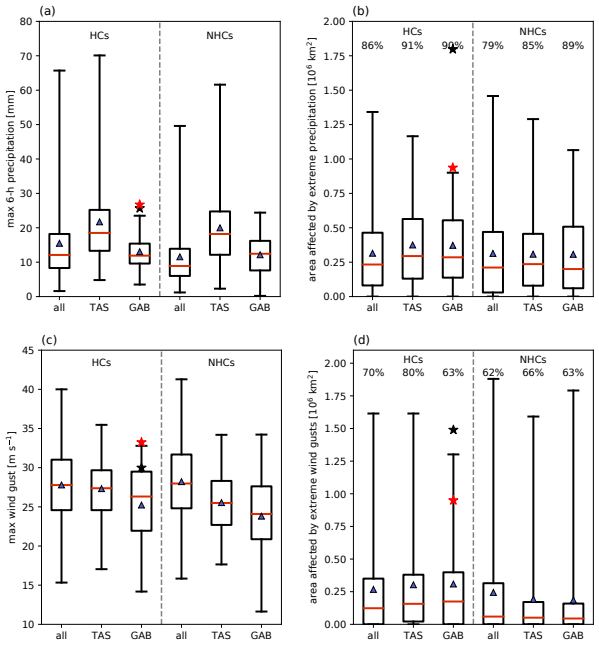

Figure 5. Box and whisker plots of (a) maximum 6-hourly precipitation, (b) area affected by extreme 6-hourly precipitation, (c) 10-m maximum wind gusts, and (d) area affected by 10-m maximum wind gusts for HCs and NHCs at the time of peak intensity. The subclasses contain all cyclones (all), cyclones over the Tasman Sea (TAS), and cyclones over the Great Australian Bight (GAB). The median is given by red lines, interquartile range by boxes, and the whiskers denote the 1 and 99th percentile, respectively. Blue triangles denote the average value. Black and red stars denote the respective values for the May and September 2016 cyclones. Percentage values denote the fraction of cyclones with extreme (b) 6-hourly precipitation and (d) wind gusts.

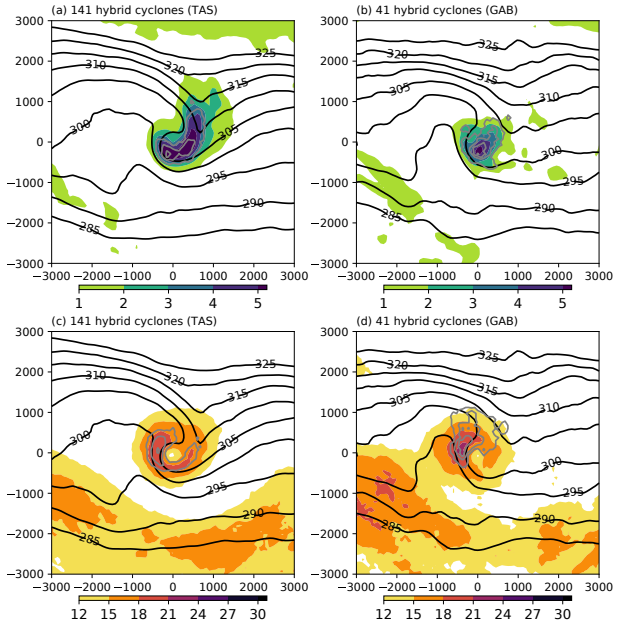

Figure 6. Composites of (a, b) mean 6-hourly accumulated precipitation (shading in mm $(6\,\mathrm{h})^{-1}$) and (c, d) mean 10-m wind gusts (shading in $\mathrm{m\,s^{-1}}$) for HCs over the (a, c) Tasman Sea (TAS) and (b, d) Great Australian Bight (GAB) at peak intensity. Grey contours denote the percentage of cyclones at which the 99th percentile of the respective quantity is exceeded (contour interval is 10%). Black contours show the 850-hPa equivalent potential temperature (every 5 K). Coordinates are given in km relative to the cyclone centre.

lower over the Great Australian Bight, they are still extreme. In 90% of the cases, HCs and NHCs are associated with extreme precipitation at least at one grid point inside the cyclone mask at their peak intensity (percentage values in Fig. 5b). Similar values can be found for cyclones over the Tasman Sea. The area affected by extreme precipitation does not differ significantly between HCs and NHCs (Fig. 5b). On average, the affected area reaches similar values for cyclones over the Tasman Sea and for those over the Great Australian Bight. The area affected by extreme precipitation exceeds the 99th percentile of all HCs over the Great Australian Bight for the May and September 2016 cyclone (red and black star in Fig. 5b). The area affected by extreme precipitation for the May cyclone is remarkable and due to the cloud band that extended over the continent.

Although the vertical thermal structure of HCs implies stronger near-surface wind than for cold core NHCs, the 10-m maximum wind gusts associated with HCs and NHCs do not differ significantly. This result is valid both when considering all cyclones and when considering cyclones over the Tasman Sea or the Great Australian Bight separately (Fig. 5c). The maximum wind gusts associated with the September 2016 cyclone exceeded the 99th percentile of maximum wind gusts for all HCs over the Great Australian Bight (red star in Fig. 5c). Generally speaking, cyclones over the Tasman Sea tend to be associated with higher maximum 10-m wind gusts than cyclones over the Great Australian Bight. For example, 80% of HCs in the Tasman Sea are associated with extreme wind gusts, whereas only 63% of HCs over the Great Australian Bight are associated with extreme wind gusts (Fig. 5d). Even though the maximum wind gusts are of similar magnitude for HCs and NHCs, the area affected by extreme wind gusts is significantly larger at the 99th percentile confidence interval in HCs than for NHCs (Fig. 5d) according to a Mann-Whitney-U test. For HCs occurring over the Great Australian Bight, the May 2016 cyclone was exceptional as the area affected by extreme wind gusts exceeded the 99th percentile for that region (black star in Fig. 5d).

That HCs over the Tasman Sea are associated with stronger precipitation than HCs over the Great Australian Bight is also evident in composite plots of mean 6-hourly precipitation at the time of their peak intensity (Figs. 6a, b). For HCs over the Tasman Sea, the strongest 6-hourly mean precipitation (shading in Fig. 6a) occurs in the warm-sector east of the HC centre and on the poleward flank in the vicinity of a bent-back warm front which is indicated by the equivalent potential temperature field (black

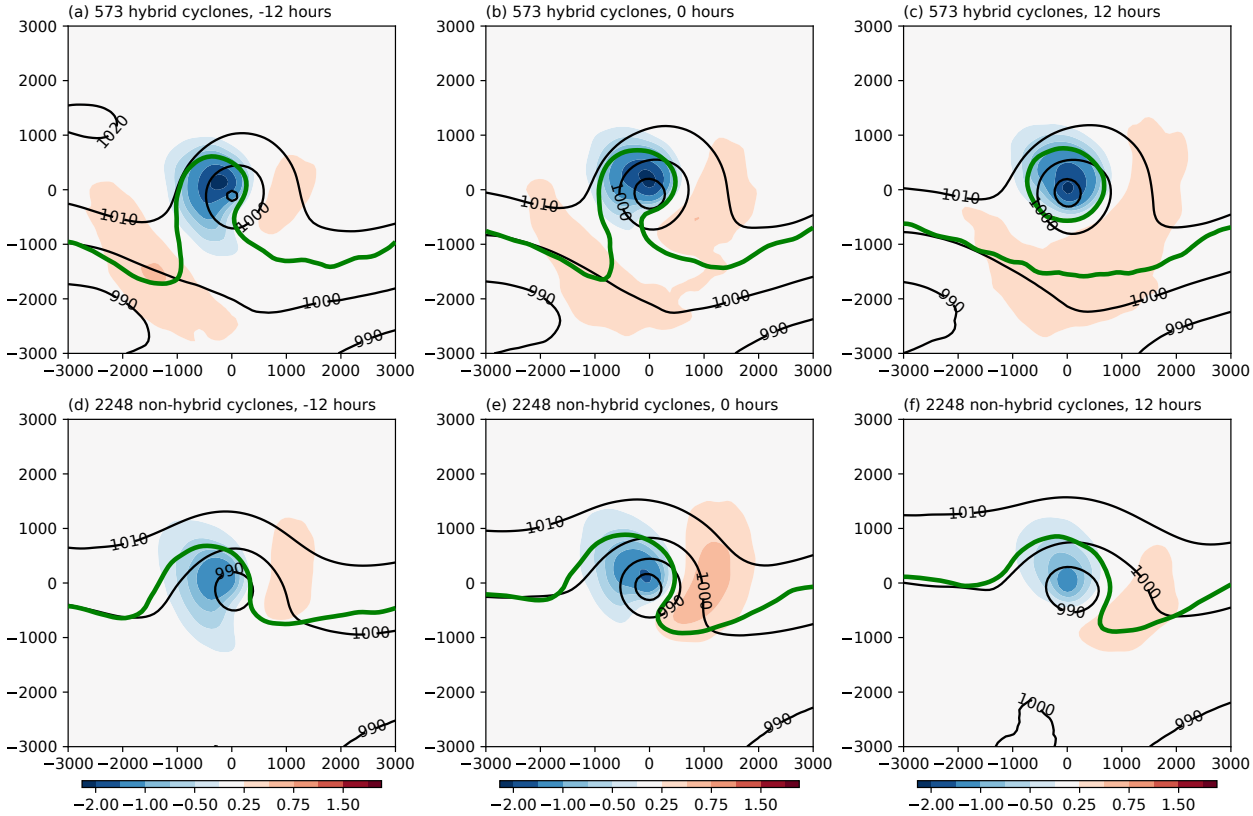

Figure 7. Composite fields of all (a-c) HCs and (d-f) NHCs during MJJAS at –12 h, 0 h, and 12 h relative to the time of peak intensity. 315-K PV anomaly relative to the monthly climatology (shading in PVU), the –2-PVU contour at 315 K (green contour), and mean sea level pressure (black contours in hPa). Coordinates are given in km relative to the cyclone centre.

contours in Fig. 6a). In particular, the precipitation along the bent-back warm front is extreme since up to 30% of the HCs over the Tasman Sea exceed the 99th percentile at the same location relative to the cyclone centre. For HCs over the Great Australian Bight (Fig. 6b), the strongest mean precipitation is confined to the warm sector and the poleward flank of the cyclone where it exceeds the 99th percentile in up to 40% of the cases.

In terms of wind gusts, the wind field associated with HCs over the Tasman Sea (Fig. 6c) appears to be more symmetric than that of HCs over the Great Australian Bight (Fig. 6d). At peak intensity, composite mean wind gusts of more than 18 m s^{-1} occur along the bent-back warm front and in the cold air mass in the wake of the cyclones over the Tasman Sea. These winds are extreme in up to 30% of the cases. Strongest winds related to HCs over the Great Australian Bight can be found in the cold air mass in the wake of the cyclone (Fig. 6d). Here, the composite mean wind gusts of more than 21 m s^{-1} exceed the 99th percentile in more than 30% of the cases.

4.3. *Cyclone structure*

Both HCs in May and September were associated with a highly amplified flow involving the formation of a meridionally elongated trough. This raises the question concerning the environmental flow in which HCs in the Australian region typically develop. This question is addressed in the following by analysing composite fields for HCs and comparing them against composite fields for NHCs.

The composite 315-K PV for all HCs in MJJAS reveals a highly amplified flow at –12 h relative to the time of peak intensity with a south–north elongated trough flanked by two ridges upstream and downstream (green contour in Fig. 7a). The trough is collocated with a cyclonic PV anomaly of less than –2 PVU compared to the monthly climatology (shading in Fig. 7a). The most anomalous cyclonic PV can still be found slightly equatorward and upstream of the low-level cyclone centre (black contours in Fig. 7a), indicating favorable conditions for a further baroclinically driven intensification.

At the time of peak intensity, the upper-level cyclonic PV anomaly is collocated in west–east direction with a low-level cyclonic PV anomaly, forming a troposphere-spanning PV-tower

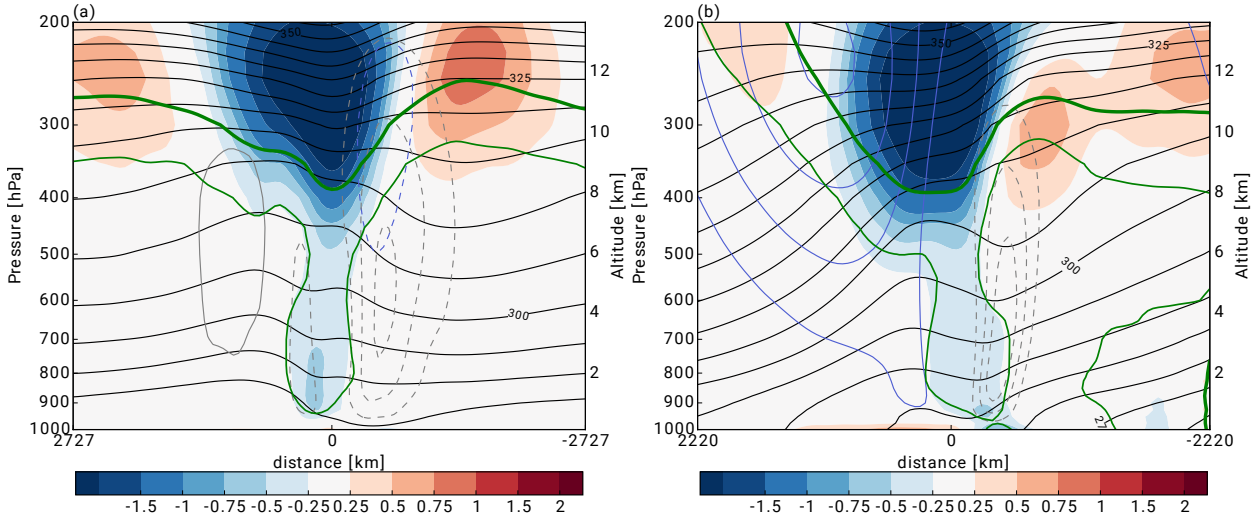

Figure 8. Composite vertical cross-section of all HCs from (a) west to east and (b) north to south at peak intensity. PV anomaly relative to the monthly climatology (shading in PVU), PV (green contours at –0.7 and –2 PVU) potential temperature (black contours every 5 K), wind speed perpendicular to cross section (blue contours every 10 m s^{-1} starting at ±20 m s^{-1}), and vertical velocity (gray contours every 0.1 Pa s^{-1}). Coordinates are given in km relative to the cyclone centre.

(green contours and shading in Fig. 8a). At 315-K the median PV anomaly reaches –2 PVU with the 10th and 90th percentile extending from –4 to about –0.2 PVU (Fig. 9a). The 850-hPa PV anomaly is significantly lower reaching a median value of –0.4 PVU (Fig. 9b). The PV-tower tilts equatorward with height as the low-level cyclone centre is slightly displaced to the south of the upper-level cyclonic PV anomaly (Fig. 8b). As with the two case studies, the subtropical jet (blue contours in Fig. 8b) is located on the equatorward flank of this cyclonic PV anomaly. The upstream ridge weakens slightly compared to 12 hours before, whereas the downstream ridge and its associated anticyclonic PV anomaly intensify (Fig. 7b). This intensification of the downstream ridge is particularly noticeable poleward of the cyclone centre where the trough is thinning considerably. The horizontal juxtaposition of anomalously cyclonic PV equatorward of the low-level cyclone centre and anomalously anticyclonic PV on its poleward side leads to a characteristic inverted treble clef (in the Southern Hemisphere) structure (e.g., Martin 1998; Posselt and Martin 2004). There are two parts to the interpretation of the treble clef structure. First, consistent with the cyclonic upper-tropospheric PV anomaly, tropospheric isentropes bend upward immediately equatorward of the cyclone centre, indicative of a column of relatively cold air (black contours in Fig. 8b). In contrast, regions of anticyclonic PV immediately poleward of the cyclone centre are associated with downward bowing isentropes indicating a column of relatively warm air. Thus, the treble clef structure is the signature of an occluded structure in the

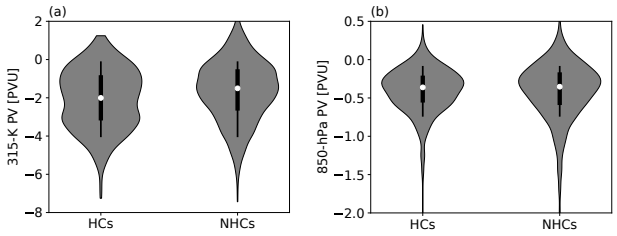

Figure 9. Violin-plot of (a) the 315-K and (b) 850-hPa PV anomaly relative to the monthly climatology for HCs and NHCs in a radius of 200 km around the cyclone centre at the time of peak intensity. White filled circles indicate median values, the vertical black thick bar denotes the interquartile range, and the black vertical line indicates the 10th and 90th percentile.

lower troposphere (Martin 1998) coinciding with the structure of the low-level equivalent potential temperature field (Fig. 6). Second, consistent with strong ascent (grey contours in Fig. 8b), it indicates the presence of diabatic processes, especially latent heat release, which intensify the notch of the treble clef by dilution of upper-tropospheric PV (Posselt and Martin 2004). Overall, the structure of the average HC at peak intensity is similar to the previously reported case studies of HCs in the Australian region (Griffiths *et al.* 1998; Mills *et al.* 2010), and the two case studies presented in Section 3.

At 12 h after peak intensity, the 315-K cyclonic PV associated with the cyclone has cut-off from the main stratospheric cyclonic PV reservoir (Fig. 7c). This PV cut-off is nearly vertically aligned with the cyclone centre terminating the intensification of the cyclone.

Although a relatively clear picture of the structure of HCs and the flow in which they are embedded emerges from this composite view, there is still a considerable case to case variability of the upper-level PV structure. The principal structures associated with

this variability among the 573 HCs can be expressed through an empirical orthogonal function (EOF) analysis of the 315-K PV anomaly in a radius of 2000 km around the cyclone centres. The three leading EOFs contain 32% of the total variance. The first EOF which contains 14% of the variability is a dipole centered between the upstream ridge and the meridionally elongated trough (Fig. 10a). Thus, in a positive sense, the first EOF defines a less intense upstream ridge but a strengthened ridge immediately south and east of the cyclone centre. Accordingly, in a negative sense, the first EOF corresponds to a highly amplified upstream ridge and a less amplified ridge southeast of the cyclone centre. Most of the variability associated with the second EOF is related to the amplitude of the ridges upstream and downstream of the cyclone (Fig. 10b). In a positive sense, enhanced ridges upstream and downstream of the cyclone centre are linked to an equatorward shift of the cyclonic PV anomaly, likely related to the formation of a PV cut-off. The third EOF still contains 7% of the variability (Fig. 10c). Its structure is less clear, although it points to a weaker downstream ridge in events of a strongly positively tilted trough. The information of this EOF analysis is used in a companion paper to separate all HCs into four clusters, and to address the question how the upper-level PV structure affects the intensity and motion of HCs.

Composites for the remaining 2248 NHCs reveal that these cyclones reach their peak intensity in a less amplified flow. At –12 h (Fig. 7d), a cyclonic PV anomaly of less than –1 PVU associated with a broad upper-level trough lies upstream of the cyclone centre providing favorable conditions for intensification. The upper-level cyclonic PV anomaly is less pronounced than for the HCs, which is likely due to a weaker upstream ridge and reduced equatorward advection of anomalous cyclonic PV air from high latitudes. For instance at the 315-K isentropic level, the median PV anomaly reaches values of –1.5 PVU (Fig. 9a) and thus is significantly less cyclonic than the median PV anomaly of HCs according to a Mann-Whitney-U test. The mean sea level pressure minimum is nearly collocated with the most cyclonic upper-level PV (Fig. 7e). The cyclone in the composite field deepens from 990 hPa to less than 980 hPa at peak intensity time and is thus about 10 hPa deeper than the average HC (cf. Figs. 7b, e). Since NHCs occur further poleward than HCs (49° S for NHCs, 41° S for HCs), the lower sea level pressure of NHCs compared to HCs does not necessarily indicate that NHCs are more intense in terms of near-surface wind speed (see also Fig. 5c). The lower mean sea level pressure is rather due to the climatologically lower values at higher latitudes. That the intensity of NHCs and HCs does not differ significantly is confirmed when analysing the lower tropospheric PV anomaly around the cyclone centre. The distributions of the 850-hPa PV anomaly do not differ significantly at the time of maximum intensity (Fig. 9b).

A pronounced upper-level ridge of slightly greater than 0.5 PVU has developed downstream of the cyclone centre, which is potentially enhanced by diabatic processes in the warm-sector of the cyclone. The upper-level PV anomalies as well as the cyclone itself weaken until 12 h (Fig. 7f). The collocation of the most cyclonic upper-level PV and of the cyclone centre indicate a termination of the cyclone development. Accordingly, the sea level pressure at the cyclone centre increases to values greater than 980 hPa.

5. Concluding discussion

Two cases of explosive hybrid cyclogenesis over the Great Australian Bight in May and September 2016 motivate the compilation of the first climatology of this type of cyclones in the Australian region. From 1979 to 2010, 1014 HCs, which are characterised by a symmetric lower-tropospheric warm core and an upper-tropospheric cold core, are identified in the ERA-Interim reanalyses using cyclone tracking and phase space diagnostics. The frequency of these cyclones shows a pronounced seasonal cycle with a peak in the Southern Hemisphere winter. During extended winter (MJJAS), HCs are most frequent over the Great Australian Bight and the Tasman Sea where they account for nearly 50% of all cyclones. In the East Coast Low region, the fraction is 6–7% higher. That most hybrid cyclones in the Tasman Sea occur during Southern Hemisphere winter is consistent with previous climatologies of subtropical cyclones and East Coast Lows for the same region (e.g., Braun 2009; Speer *et al.* 2009; Browning and Goodwin 2013).

Previous case studies, as well as the two motivating events, suggest that HCs may be more extreme in their precipitation and near-surface winds than NHCs in the same region. Although 91%

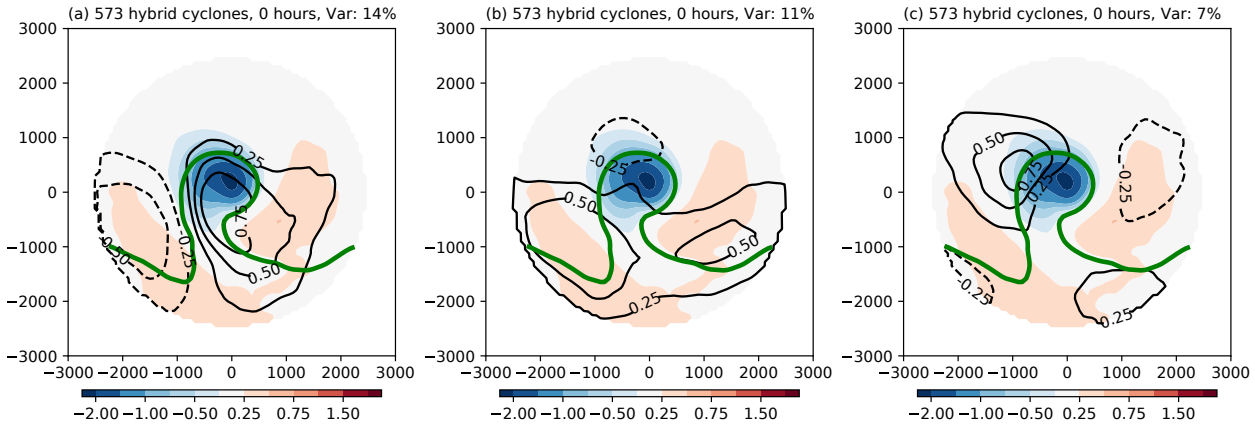

Figure 10. Composite fields of all HCs as in Fig. 7 at the time of peak intensity, except for the black contours showing (a) EOF1, (b) EOF2, and (c) EOF3 of the 315-K PV anomaly (contour interval 0.25 PVU). The variance explained by each EOF is given in the subcaptions. Coordinates are given in km relative to the cyclone centre.

of the HCs in MJJAS are associated with extreme precipitation, the magnitude and the area affected by precipitation extremes do not differ significantly from NHCs. Instead, it is the geographical region that determines the magnitude of the precipitation. For example, cyclones in the Great Australian Bight tend to be associated with systematically less precipitation than those over the Tasman Sea. This result is likely due to higher SSTs in the Tasman Sea than in the Great Australian Bight and reduced moisture over the continent which can be transported into the warm sector of the cyclones in the Great Australian Bight. That the most extreme precipitation typically occurs on the poleward flank of the cyclones and along the bent-back warm front corroborates previous case studies and climatologies on East Coast Lows (Mills *et al.* 2010; Pepler *et al.* 2017a) and hybrid cyclones over other ocean basins (e.g., Simpson 1952; Davis and Bosart 2004; Hulme and Martin 2009). Also, the magnitude of the maximum near-surface wind gusts does not differ significantly between HCs and NHCs. However, the area affected by extreme wind gusts associated with HCs is significantly larger than that of NHCs. The strongest wind gusts typically occur in the cold air mass to the west of the cyclone centre and, for HCs over the Tasman Sea, along the bent-back warm front. The latter result is consistent with the satellite-based climatology by Pepler *et al.* (2017a).

The case studies for the May and September 2016 cyclones, as well as composite fields for all 573 HCs during extended winter (May–September), show that the average HC in the Australian region reaches peak intensity in an amplified flow including upper-tropospheric ridges upstream and downstream of the cyclone as well as a south–north elongated trough. This supports previous case studies (e.g., Griffiths *et al.* 1998; Garde *et al.* 2010; Mills *et al.* 2010; Cavicchia *et al.* 2018) as well as composite analyses of East Coast Lows (e.g., Browning and Goodwin 2013; Dowdy *et al.* 2013). At peak intensity, HCs are characterised by a troposphere-spanning PV-tower which tilts equatorward with height. This equatorward tilt with height has been noted for cyclones in general occurring south of Australia (Lim and Simmonds 2007). The elongated trough develops a characteristic inverted treble clef (in the Southern Hemisphere) structure due to ridge-building immediately downstream. Around 12 hours after the peak intensity, the upper-level PV associated with the HC detaches from the main stratospheric PV reservoir and forms a PV cut-off that is collocated with the cyclone centre. This characteristic development has been noted for hybrid cyclones in other ocean basins (e.g., Moore *et al.* 2008; Posselt and Martin 2004) and over the Tasman Sea (Garde *et al.* 2010). In contrast to HCs, NHCs develop in a flow that is considerably less amplified upstream of the cyclones and the associated upper-tropospheric trough does not develop into a PV cut-off. An EOF analysis reveals that much of the variability of the upper-tropospheric PV structure among all HCs is related to the amplitude of the ridges upstream and downstream of the cyclones. The identified case-to-case variability motivates a companion study in which all HCs are separated into four distinct clusters in order to address the question on how the environmental upper-level PV structure affects the intensity and motion of HCs.

The conclusions drawn from the present study are valid only for HCs in the Australian region. Hence, an intriguing research opportunity may be to extend the analysis to the global scale and

to elaborate regional differences concerning the structure of HCs and their link to precipitation and wind extremes.

Acknowledgement

We are thankful to Duncan Ackerley, Lance Bosart and Christian Grams for inspiring discussions and helpful comments on an earlier version of this manuscript, to Acacia Pepler for providing the East Coast Low data set, and to Heini Wernli and an anonymous reviewer for providing encouraging comments which greatly improved the manuscript. The contribution of JFQ was partly funded by the Helmholtz-Association (grant VH-NG-1243). MJR gratefully acknowledges funding provided by the Australian Research Council Centre of Excellence for Climate Extremes (CE170100023). JLC was funded by the ARC Discovery Early Career Researcher Award grant DE140101305. We thank the Australian National Computational Infrastructure and ECMWF for providing access to the ERA-Interim reanalysis data.

References

Bentley AM, Metz ND. 2016. Tropical transition of an unnamed, high-latitude, tropical cyclone over the eastern North Pacific. *Monthly Weather Review* **144**(2): 713–736, doi:10.1175/MWR-D-15-0213.1.

Bjerknes J, Solberg H. 1922. Life cycle of cyclones and the polar front theory of atmospheric circulation. *Geofys. Publ.* **3**(1): 3–18.

Braun AJ. 2009. A comparison between South Atlantic and Tasman Sea subtropical storms. M.s. thesis, Department of Meteorology, The Pennsylvania State University, University Park, PA.

Browning KA, Hill FF. 1985. Mesoscale analysis of a polar trough interacting with a polar front. *The Quarterly Journal of the Royal Meteorological Society* **111**(464): 445–462, doi:10.1002/qj.49711146409.

Browning SA, Goodwin ID. 2013. Large-scale influences on the evolution of winter subtropical maritime cyclones affecting Australia's East Coast. *Monthly Weather Review* **141**(7): 2416–2431, doi:10.1175/MWR-D-12-00312.1.

Bureau of Meteorology. 2016a. Monthly weather review Australia May 2016. Technical Report May, Bureau of Meteorology, URL `http://www.bom.gov.au/climate/mwr/aus/mwr-aus-201605.pdf`.

Bureau of Meteorology. 2016b. Monthly weather review Australia September 2016. Technical Report September, Bureau of Meteorology, URL `http://www.bom.gov.au/climate/mwr/aus/mwr-aus-201609.pdf`.

Čampa J, Wernli H. 2012. A PV perspective on the vertical structure of mature midlatitude cyclones in the Northern Hemisphere. *Journal of the Atmospheric Sciences* **69**(2): 725–740, doi:10.1175/JAS-D-11-050.1.

Caruso SJ, Businger S. 2006. Subtropical cyclogenesis over the central North Pacific. *Weather and Forecasting* **21**(2): 193–205, doi:10.1175/WAF914.1.

Catto JL, Pfahl S. 2013. The importance of fronts for extreme precipitation. *Journal of Geophysical Research: Atmospheres* **118**(19): 10,791–10,801, doi:10.1002/jgrd.50852.

Cavicchia L, Dowdy A, Walsh K. 2018. Energetics and dynamics of subtropical Australian east coast cyclones: two contrasting cases. *Mon. Weather Rev.* **146**(5): 1511–1525, doi:10.1175/MWR-D-17-0316.1.

Cordeira JM, Bosart LF. 2011. Cyclone interactions and evolutions during the "Perfect Storm" of late October and early November 1991. *Monthly Weather Review* **139**(6): 1683–1707, doi:10.1175/2010MWR3537.1.

Davis CA, Bosart LF. 2004. The TT problem. *Bulletin of the American Meteorological Society* (November): 1657–1662, doi:10.1175/BAMS-85-11-1657.

Dee DP, Uppala SM, Simmons AJ, Berrisford P, Poli P, Kobayashi S, ... Vitart F. 2011. The ERA-Interim reanalysis: Configuration and performance of the data assimilation system. *Quarterly Journal of the Royal Meteorological Society* **137**(656): 553–597, doi:10.1002/qj.828.

Dowdy AJ, Mills GA, Timbal B. 2013. Large-scale diagnostics of extratropical cyclogenesis in eastern Australia. *International Journal of Climatology* **33**(10): 2318–2327, doi:10.1002/joc.3599.

Downey WK, Tsuchiya T, Schreiner AJ. 1981. Some aspects of a northwestern Australian cloud band. *Australian Meteorological Magazine* **29**(3): 99–113.

ECMWF. 2007. IFS documentation - Cy31r1. Technical Report June, ECMWF.

Evans C, Wood KM, Aberson SD, Archambault HM, Milrad SM, Bosart LF, ...Zhang F. 2017. The extratropical transition of tropical cyclones. Part I: Cyclone evolution and direct impacts. *Monthly Weather Review* : MWR–D–17–0027.1doi:10.1175/MWR-D-17-0027.1.

Evans JL, Braun A. 2012. A climatology of subtropical cyclones in the South Atlantic. *Journal of Climate* **25**(21): 7328–7340, doi:10.1175/JCLI-D-11-00212.1.

Evans JL, Guishard MP. 2009. Atlantic subtropical storms. Part I: Diagnostic criteria and composite analysis. *Monthly Weather Review* **137**(7): 2065–2080, doi:10.1175/2009MWR2468.1.

Evans JL, Hart RE. 2003. Objective indicators of the life cycle evolution of extratropical transition for Atlantic tropical cyclones. *Monthly Weather Review* **131**(5): 909–925, doi:10.1175/1520-0493(2003)131⟨0909:OIOTLC⟩2.0.CO;2.

Evans MS, Keyser D, Bosart LF, Lackmann GM. 1994. A satellite-derived classification scheme for rapid maritime cyclogenesis. *Monthly Weather Review* **122**(7): 1381–1416.

Garde LA, Pezza AB, Tristram Bye JA. 2010. Tropical transition of the 2001 Australian Duck. *Mon. Weather Rev.* **138**(6): 2038–2057, doi:10.1175/2009MWR3220.1.

González-Alemán JJ, Valero F, Martín-León F, Evans JL. 2015. Classification and synoptic analysis of subtropical cyclones within the northeastern Atlantic Ocean. *Journal of Climate* **28**(8): 3331–3352, doi:10.1175/JCLI-D-14-00276.1.

Griffiths M, Reeder MJ, Low DJ, Vincent RA. 1998. Observations of a cut-off low over southern Australia. *Quarterly Journal of the Royal Meteorological Society* **124**(548): 1109–1132, doi:10.1002/qj.49712454805.

Grønås S. 1995. The seclusion intensification of the New Year's day storm 1992. *Tellus A* **47**(5): 733–746, doi:10.1034/j.1600-0870.1995.00116.x.

Guishard MP, Evans JL, Hart RE. 2009. Atlantic subtropical storms. Part II: climatology. *Journal of Climate* **22**(13): 3574–3594, doi:10.1175/2008JCLI2346.1.

Hart RE. 2003. A cyclone phase space derived from thermal wind and thermal asymmetry. *Monthly Weather Review* **131**(4): 585–616, doi:10.1175/1520-0493(2003)131⟨0585:ACPSDF⟩2.0.CO;2.

Hines KM, Mechoso CR. 1993. Influence of surface drag on the evolution of fronts. *Monthly Weather Review* **121**(4): 1152–1175.

Hodges KI. 1994. A general-method for tracking analysis and its application to meteorological data. *Monthly Weather Review* **122**(11): 2573–2586, doi:10.1175/1520-0493(1994)122⟨2573:AGMFTA⟩2.0.CO;2.

Hodges KI. 1995. Feature tracking on the unit sphere. *Monthly Weather Review* **123**(12): 3458–3465, doi:10.1175/1520-0493(1995)123⟨3458:FTOTUS⟩2.0.CO;2.

Hodges KI. 1999. Adaptive constraints for feature tracking. *Monthly Weather Review* **127**(6): 1362–1373, doi:10.1175/1520-0493(1999)127⟨1362:ACFFT⟩2.0.CO;2.

Holland GJ, Lynch AH, Leslie LM. 1987. Australian East-Coast Cyclones. Part I: synoptic overview and case study. *Monthly Weather Review* **115**(12): 3024–3036, doi:10.1175/1520-0493(1987)115⟨3024:AECCPI⟩2.0.CO;2.

Hoskins BJ, Hodges KI. 2002. New perspectives on the Northern Hemisphere winter storm tracks. *Journal of the Atmospheric Sciences* **59**(6): 1041–1061, doi:10.1175/1520-0469(2002)059⟨1041:NPOTNH⟩2.0.CO;2.

Hoskins BJ, Hodges KI. 2005. A new perspective on Southern Hemisphere storm tracks. *Journal of Climate* **18**(20): 4108–4129, doi:10.1175/JCLI3570.1.

Hulme AL, Martin JE. 2009. Synoptic- and frontal-scale influences on tropical transition events in the Atlantic basin. Part II: Tropical transition of Hurricane Karen. *Monthly Weather Review* **137**(11): 3626–3650, doi:10.1175/2009MWR2803.1.

Jones SC, Harr PA, Abraham J, Bosart LF, Bowyer PJ, Evans JL, . . . Thorncroft C. 2003. The extratropical transition of tropical cyclones: Forecast challenges, current understanding, and future directions. *Weather and Forecasting* **18**(6): 1052–1092, doi:10.1175/1520-0434(2003)018⟨1052:TETOTC⟩2.0.CO;2.

Knapp KR, Ansari S, Bain CL, Bourassa MA, Dickinson MJ, Funk C, . . . Magnusdottir G. 2011. Globally gridded satellite observations for climate studies. *Bulletin of the American Meteorological Society* **92**(7): 893–907, doi:10.1175/2011BAMS3039.1.

Lim EP, Simmonds I. 2007. Southern Hemisphere winter extratropical cyclone characteristics and vertical organization observed with the ERA-40 data in 1979-2001. *Journal of Climate* **20**(11): 2675–2690, doi:10.1175/JCLI4135.1.

Lucas A. 2017. Confected conflict in the wake of the South Australian blackout: Diversionary strategies and policy failure in Australia's energy sector. *Energy Research and Social Science* **29**(December 2016): 149–159, doi:10.1016/j.erss.2017.05.015.

Martin JE. 1998. The structure and evolution of a continental winter cyclone. Part I: Frontal structure and the occlusion process. *Monthly Weather Review* **126**(2): 303–328, doi:10.1175/1520-0493(1998)126⟨0303:TSAEOA⟩2.0.CO;2.

McTaggart-Cowan R, Galarneau TJ, Bosart LF, Moore RW, Martius O. 2013. A global climatology of baroclinically influenced tropical cyclogenesis. *Monthly Weather Review* **141**(6): 1963–1989, doi:10.1175/MWR-D-12-00186.1.

Mills GA. 2001. Mesoscale cyclogenesis in reversed shear – the 1998 Sydney to Hobart yacht race storm. *Australian Meteorological Magazine* **50**(1): 29–52.

Mills GA, Webb R, Davidson NE, Kepert J, Seed A, Abbs D. 2010. The Pasha Bulker east coast low of 8 June 2007. Technical Report June, CAWCR.

Mills GA, Wu BJ. 1995. The 'Cudlee Creek' flash-flood – an example of synoptic-scale forcing of a mesoscale event. *Australian Meteorological Magazine* **44**(3): 201–218.

Moore RW, Martius O, Davies HC. 2008. Downstream development and Kona low genesis. *Geophysical Research Letters* **35**(20): 1–6, doi:10.1029/2008GL035502.

Neiman PJ, Shapiro MA. 1993. The life cycle of an extratropical marine cyclone. Part I: frontal-cyclone evolution and thermodynamic air-sea interaction. *Mon. Wea. Rev.* **121**(8): 2153–2176, doi:10.1175/1520-0493(1993)121⟨2153:TLCOAE⟩2.0.CO;2.

Otkin JA, Martin JE. 2004. A synoptic climatology of the subtropical Kona storm. *Monthly Weather Review* **132**(6): 1502–1517, doi:10.1175/1520-0493(2004)132⟨1502:ASCOTS⟩2.0.CO;2.

Pepler AS, Di Luca A, Evans JP. 2017a. Independently assessing the representation of midlatitude cyclones in high-resolution reanalyses using satellite observed winds. *International Journal of Climatology* **1327**(August 2017): 1314–1327, doi:10.1002/joc.5245.

Pepler AS, Fong J, Alexander LV. 2017b. Australian east coast mid-latitude cyclones in the 20th Century Reanalysis ensemble. *International Journal of Climatology* **37**(4): 2187–2192, doi:10.1002/joc.4812.

Pfahl S, Wernli H. 2012. Quantifying the relevance of cyclones for precipitation extremes. *Journal of Climate* **25**(19): 6770–6780, doi:10.1175/JCLI-D-11-00705.1.

Posselt D, Martin J. 2004. The effect of latent heat release on the evolution of a warm occluded thermal structure. *Monthly weather review* **132**(2): 578–599, doi:10.1175/1520-0493(2004)132⟨0578:TEOLHR⟩2.0.CO;2.

Qi L, Leslie LM, Speer MS. 2006. Climatology of cyclones over the southwest Pacific: 1992-2001. *Meteorology and Atmospheric Physics* **91**(1-4): 201–209, doi:10.1007/s11427-006-0201-8.

Qi L, Leslie LM, Zhao S. 1999. Cut-off low pressure systems over southern Australia: Climatology and case study. *International Journal of Climatology* **19**: 1633 – 1649, doi:10.1002/(SICI)1097-0088(199912)19:15⟨1633::AID-JOC445⟩3.0.CO;2-0.

Reed RJ, Kuo YH, Low-Nam S. 1994. An Adiabatic Simulation of the ERICA IOP 4 Storm: An Example of Quasi-Ideal Frontal Cyclone Development. *Monthly Weather Review* **122**(12): 2688–2708.

Rossa MA, Wernli H, Davies CH. 2000. Growth and decay of an extra-tropical cyclone's PV-tower. *Meteorology and Atmospheric Physics* **73**(3): 139–156, doi:10.1007/s007030050070.

Sanders F, Gyakum JR. 1980. Synoptic-dynamic climatology of the "bomb". *Monthly Weather Review* **108**: 1589–1606, doi:10.1175/1520-0493(1980)108⟨1589:SDCOT⟩2.0.CO;2.

Schultz DM, Keyser D, Bosart LF. 1998. The effect of large-scale flow on low-level frontal structure and evolution in midlatitude cyclones. *Monthly Weather Review* **126**(7): 1767–1791, doi:10.1175/1520-0493(1998)126⟨1767:TEOLSF⟩2.0.CO;2.

Shapiro MA, Keyser D. 1990. Fronts, jet streams and the tropopause. In: *Extratropical Cyclones: The Erik Palmen memorial volume*, Newton CW, Holopainen EO (eds), Am. Meteorol. Soc.: Boston, Mass., pp. 167–191.

Simpson RH. 1952. Evolution of the Kona Storm, a subtropical cyclone. *Journal of Meteorology* **9**(1): 24–35, doi:10.1175/1520-0469(1952)009⟨0024:EOTKSA⟩2.0.CO;2.

Snyder C, Skamarock WC, Rotunno R. 1991. A comparison of primitive-equation and semigeostrophic simulations of baroclinic waves. *Journal of the Atmospheric Sciences* **48**(19): 2179–2194, doi:10.1175/1520-0469(1991)048⟨2179:ACOPEA⟩2.0.CO;2.

Speer M, Wiles P, Pepler A. 2009. Low pressure systems off the new south wales coast and associated hazardous weather: establishment of a database. *Australian Meteorological and Oceanographic Journal* **58**(01): 29–39, doi:10.22499/2.5801.004.

Takayabu I. 1986. Roles of the horizontal advection on the formation of surface fronts and on the occlusion of a cyclone developing in the baroclinic westerly jet. *Journal of the Meteorological Society of Japan* **64**(3): 329–345.

Thorncroft CD, Hoskins BJ, McIntyre ME. 1993. Two paradigms of baroclinicwave lifecycle behaviour. *Quarterly Journal of the Royal Meteorological Society* **119**(509): 17–55, doi:10.1002/qj.49711950903.

Wang CC, Rogers JC. 2001. A composite study of explosive cyclogenesis in different sectors of the North Atlantic. Part I: cyclone structure and evolution. *Monthly Weather Review* **129**: 1481–1499, doi:10.1175/1520-0493(2001)129⟨1481:ACSOEC⟩2.0.CO;2.

Yanase W, Niino H, Hodges K, Kitabatake N. 2014. Parameter spaces of environmental fields responsible for cyclone development from tropics to extratropics. *Journal of Climate* **27**(2): 652–671, doi:10.1175/JCLI-D-13-00153.1.

Zillman JW, Price PG. 1972. On the thermal structure of mature Southern Ocean cyclones. *Australian Meteorological Magazine* **20**: 34–48.